Dear Editor,

Thank you for considering our manuscript for possible publication in Dalton Transactions. We have carefully gone through the comments of the referees, and tried to address them. We would also like to thank the referees for their input. We believe their comments have been very valuable and helped in further improving the manuscript. Below, we have listed our response to the comments, while the changes in the manuscript have been highlighted in red.

Reviewer's comments:

Reviewer #1:

The manuscript focuses on the preparation of Nickel and Cobalt Phosphate by Plasma Enhanced Atomic Layer Deposition, especially for Nickel Phosphate, and their electrochemical performances as lithium ion batteries cathode. This work is significant, whereas the structural characterization is weak. Thus, I think this manuscript can be published in Dalton Transactions after major revisions.

(1) Please provide the SEM, AFM and TEM characterizations of the Ni3(PO4)2 and Ni2P thin films

Response: Thank you for the suggestions. Unfortunately, we do not have a TEM available at our lab, so we were not able to perform such measurements. We did include a SEM and AFM analysis of the as deposited and annealed films, showing that the material agglomerates during the crystallisation into both $Ni_3(PO_4)_2$ and Ni_2P. The increase in roughness showed to be the highest for the nickel phosphide layers (i.e. the anneal in a hydrogen atmosphere).

(2) Please provide the detailed preparation process of Ni3(PO4)2 and Ni2P thin film electrode

Response: The crystalline nickel phosphate and phosphide were obtained by annealing the as deposited layer in a helium and hydrogen atmosphere respectively. The annealing rate was however not mentioned in the text so far, so this has been added. An additional safety concern related to the formation of phosphine gas during the anneal in hydrogen has also been added.

For the nickel phosphate battery electrode, the as-deposited material resulting from the saturated ALD process (so not the crystalline $Ni_3(PO_4)_2$ or Ni_2P) was deposited on top of a current collector. This information has also been added to the manuscript.

(3) Some related references about ALD and Batteries should be cited, such as: Controllable atomic layer deposition coatings to boost the performance of LiMnxCoyNi1-x-yO2 in lithium-ion batteries: A review. J. Mater. Res., 2020, 35(7): 762-774 (DOI: 10.1557/jmr.2019.393); Chemical Heterointerface Engineering on Hybrid Electrode Materials for Electrochemical Energy Storage. Small Methods, 5(8): 2021, 202100444 (DOI: 10.1002/smtd.202100444).

Response: Thank you for the suggestions. These articles, amongst others, have been added to the introduction.

We would like to thank the reviewer for the valuable input. We believe that the suggestions served a great deal in further improving the manuscript.

Reviewer #2:

In this paper, the authors used ALD to deposit metal phosphates for lithium-ion batteries. The procedures and properties of deposited materials are thoroughly discussed. The performance in lithium-ion batteries is promising. However, the following aspects need to be clarified before acceptance.

(1) The authors report about several crucial parameters for the ALD process. As it is an engineering procedure, the error bar for each parameter is important to warrant the reproducibility.

Response: Two important properties of the ALD process/final layer are the growth rate and the final composition. For the latter material property, the error on the ERD values are presented in the experimental section. For the growth per cycle, we have to split the question in two parts. On the one hand, there is the error on the ellipsometry measurement (i.e. the datapoints in the saturation curve). Each data point in these curves is the average growth per cycle over the course of 10 cycles, within one deposition. The error on these datapoints shows relatively small, and we have included a figure here to illustrate this. This shows that the error on the ellipsometry data is relatively small.

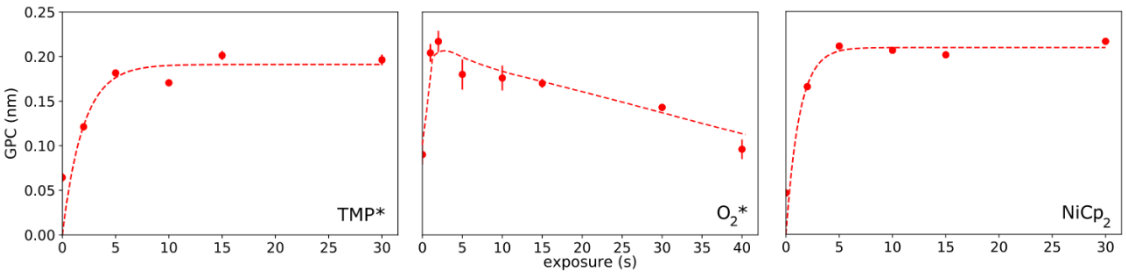

On the other hand, there also is the variation of the growth per cycle over the course of different depositions. Thanks to this comment, we have added an average optimised growth per cycle in the manuscript (with saturated exposure times for TMP* and $NiCp_2$, and 15s of O_2*) with the error over the course of 4 different depositions.

(2) The excessive charge (5.7 vs. 4.8) is observed for the first cycle. How about the following charge/discharge cycles? Do they obey the theoretical calculation?

Response: In the supporting information, the capacity of the anodic scan following the activation is discussed. The possible reaction mechanisms are explained, as well as how close the capacity is to the theoretical values for those reactions. The capacity of the following discharge was not yet discussed. However, as can be seen from our latest cycle life measurement, we achieve a coulombic efficiency of approximately 98% in the example of nickel phosphate. The charge and discharge capacity are thus very similar, indicating reversible reactions after the activation step.

(3) The unit of y-axis of Figure 7b implies ultralow capacity, less than 10⁻⁵ μAh/cm². However, the capacity reported in the main text show several μAh/cm².

Response: Thank you for noticing. We have made a mistake with the y-axis label in figure 7b, and this was overlooked until now. The dimensions on the y-axis are supposed to be in Ah/cm^2 instead of $\mu Ah/cm^2$. This has been addressed in the manuscript.

(4) Rate performance is demonstrated. The cycling performance, an important parameter to evaluate the material performance, is missing.

Response: This is indeed an important parameter to evaluate when thinking of their use as an LIB electrode. For iron phosphate, the cycle life has already been measured in an earlier publication (DOI: 10.1021/acs.chemmater.6b00853) and was thus not measured here. For nickel and cobalt phosphate, however, this was not yet measured. We have added this analysis in the manuscript, showing that the nature of the redox reaction probably leads to a non-ideal cycle life, although it is still decent.

Thank you for the comments and suggestions. The additional measurements and corrections that were proposed have had, in our opinion, a very positive impact on the quality of the manuscript.

Plasma Enhanced Atomic Layer Deposition of Nickel and Cobalt Phosphate for Lithium Ion Batteries

Lowie Henderick,[†] Ruben Blomme,[†] Matthias Minjauw,[†] Jonas Keukelier,[†] Johan Meersschaut,[‡] Jolien Dendooven,[†] Philippe Vereecken,[‡] and Christophe Detavernier*[,†]

†*Department of Solid State Sciences, Ghent University, Krijgslaan 281 S1, 9000 Gent, Belgium*

‡*imec, Kapeldreef 75, B-3001 Heverlee, Belgium*

E-mail: Christophe.Detavernier@Ugent.be

Abstract

A plasma-enhanced ALD process has been developed to deposit nickel phosphate. The process combines a trimethylphosphate (TMP) plasma with an oxygen plasma and nickelocene at a substrate temperature of 300°C. Saturation at a growth per cycle of approximately 0.2 nm/cycle is observed for both the TMP plasma and nickelocene, while a continuous decrease in the growth per cycle is found for the oxygen plasma. From ERD, a stoichiometry of $Ni_3(P_{0.8}O_{3.1})_2$ is measured, but by adding an additional oxygen plasma after the nickelocene, the composition of $Ni_3(P_{0.9}O_{3.7})_2$ becomes even closer to stoichiometric $Ni_3(PO_4)_2$. The as deposited layer resulting from the process without the additional oxygen plasma is amorphous, but can be crystallised into Ni_2P or crystalline $Ni_3(PO_4)_2$ by annealing in hydrogen or helium atmosphere respectively. The layer deposited with the additional

oxygen plasma shows two X-ray diffraction peaks indicating the formation of crystalline $Ni_3(PO_4)_2$ already during the deposition. The resulting PE-ALD deposited nickel phosphate layers were then electrochemically studied and compared to PE-ALD cobalt and iron phosphate. All phosphates need electrochemical activation at low potential first, after which reversible redox reactions are observed at a potential of approximately 2.5 V vs. Li^+/Li. A relatively high capacity and good rate behaviour are observed for both nickel and cobalt phosphate, which are thought to originate from either a conversion type reaction or an alloying reaction.

Introduction

Since the introduction of iron phosphate as a Li-ion battery (LIB) electrode by Sony in 1991, transition metal phosphates have played an important role in various research fields[1–3]. A major advantage for the use of phosphates in LIB's in particular, is the strong covalency in the metal-oxygen-phosphorus bonds allowing for a high structural and thermal stability.[4] Next to this, the strong interaction between the metal atom and the phosphate anion allow for these materials to operate at a higher potential than their oxide counterparts.[2,5] However, the energy density of the most known metal phosphate, i.e. iron phosphate, is still limited. For that reason, other phosphates are being actively investigated for both current (lithium ion[2]) and future generation (sodium ion[2,4]) batteries. In this view, the use of nickel and cobalt phosphate as electrode materials (operating at a much higher potential) are currently gaining a lot of interest. Theoretical studies predict the operating voltage of the Ni^{2+}/Ni^{3+} redox couple in olivine nickel phosphate to be at approximately 5.1 V vs Li^+/Li and the Co^{2+}/Co^{3+} redox couple in olivine cobalt phosphate at approximately 4.6 V vs Li^+/Li.[6] However, although some functional nickel- and/or cobalt phosphate electrodes have been reported, these are still scarce as both materials suffer from various issues such as instability (of both the electrode and its interface with the electrolyte) at these high potentials and poor electronic conductivity. Various possible solutions have been proposed in the form of

surface coatings[7], doping[8,9] or enhanced synthesis methods[10], but more research is needed in order to commercialise these electrode materials.

Another interesting use for both materials would be towards surface engineering of other cathode materials, such as lithium nickel manganese cobalt oxide (NMC), that operate at slightly lower potential. When using a surface coating, often inert materials such as aluminium oxide are used as a physical barrier layer to prevent unwanted side reactions to take place.[11] However, these coatings typically have a poor ionic conductivity, imposing serious limits on the rate capability of the underlying electrode.[12] For that reason, it would be interesting to work with a coating that has a higher ionic conductivity, which might even locally take up a functional role transporting lithium ions along the surface of the active material (enhancing the reachability of more isolated particles). As the delithiation of nickel and cobalt phosphate would take place at a potential above the operating potential of the underlying electrode, the coating will remain permanently lithiated. This could boost the ionic conductivity, rendering these materials very interesting to further investigate.

An interesting way to study and optimise both materials towards their use for LIB applications can be through atomic layer deposition (ALD).[13] ALD is a deposition technique based on the sequential pulsing of gaseous precursors, similar to chemical vapour deposition (CVD). The key difference with a typical CVD process is however that the reactions taking place at the surface of the substrate during an ALD process are self-limiting. This self-limiting nature of the reactions during deposition not only allows for a high control on thickness, uniformity and conformality of the coating, but also its composition. One way this deposition technique could be of interest for LIB's is through the deposition of a thin film electrode[14,15] onto a complex 3D structured current collector, allowing for an electrode providing a high overall capacity with an excellent power density. Next to this, the technique can be used to conformally coat e.g. powder-based electrode materials with a protective thin

film[14–17]. In this regard, various metal phosphates have for example already been proven very promising towards improving the final electrode's performance[18–20]. However, the study of thin films in general also offers a unique way to create model systems to gain a fundamental insight towards a broad range of applications. In that way, the study of nickel phosphate through ALD can be of interest towards various research fields.

However, so far no ALD process exists for nickel phosphate. In this work, an initial attempt towards researching ALD of nickel phosphate will be made based on earlier work by Dobbelaere et al.[21]. In this work, aluminium phosphate was deposited through a plasma enhanced ALD process (PE-ALD), combining a trimethylphosphate plasma (TMP*, with the star denoting the plasma state) with an oxygen plasma and trimethylaluminum (TMA). However, it was quickly found that by changing the metal precursor, other metal phosphates such as titanium[22], vanadium[23], zinc[24], iron[25] and cobalt phosphate[26] could be deposited as well. For the deposition of nickel phosphate in this work, the metalorganic precursor of choice became nickelocene, inspired by our earlier work on PE-ALD of cobalt phosphate and as this precursor has already proven successful towards PE-ALD of nickel oxide.[27]
Next to studying the deposition of this nickel phosphate, its electrochemical activity will be investigated together with PE-ALD deposited cobalt phosphate (resulting from the already reported PE-ALD process[26]) and compared to the already reported PE-ALD deposited iron phosphate for reference. In this work, only the electrochemical activity of both layers will be studied (i.e. not yet their potential use as an LIB cathode coating), as a first step for the use of these ALD deposited layers in LIB applications.

Experimental section

Deposition system. A home-built high-vacuum ALD system with a base pressure of approximately $5 * 10^{-6}$ mbar was used to deposit the films, for which the reactor design is very similar to

the system used in the work by Dobbelaere et al.[25] To reach this base pressure, the reactor walls were heated up to 120 °C and the chamber was pumped with a turbomolecular pump. The TMP (Sigma-Aldrich, 97%) and $CoCp_2$ (Alfa Aesar) precursor bottles were heated up to 45 °C and 105 °C, while a manually adjustable needle valve was installed to control the pressure of the oxygen gas at a value of approximately $5 * 10^{-3}$ mbar. $NiCp_2$ (Strem chemicals, 99%) was heated up to 75 °C, and its vapour was introduced in the reactor using argon at a pressure of $5 * 10^{-3}$ mbar as carrier gas. The plasma power was selected to be 200 W for TMP and 300 W for the oxygen plasma. The plasma was delivered to the sample surface using a remote ICP-RF plasma located above the sample surface.

Material characterization. In situ spectroscopic ellipsometry was performed using a J.A. Woollam M-2000 ellipsometer, while fitting was done using the CompleteEASE software. Film thickness was measured on p-type Si(100) using X-Ray Reflectivity (XRR). Both XRR and X-Ray Diffraction (XRD, in a Bragg-Brentano θ:θ geometry) were carried out using a Bruker D8 diffractometer Cu Kα radiation. X-Ray Photoelectron spectroscopy (XPS) was performed using a Thermo Scientific Theta Probe XPS and Al Kα radiation. Calibration of the XPS spectra was performed using the C 1s position at 284.6 eV. The spectra that are shown in the manuscript were measured at the surface of the as deposited thin film. Elastic Recoil Detection[28] (ERD) was carried out using a 8.0 MeV $^{35}Cl^{4+}$ beam, with a sample tilt of 15° and a scatter angle of 40.5°. The uncertainty on the atomic concentration measured with ERD is 2 at.% for majority constituents ($>$ 15 at.%), 1 at.% for concentrations between 7 at.% and 15 at.%, 0.7 at.% for concentrations below 7 at.% and 0.3 at.% for concentrations below 3 at.%. For hydrogen, there is an additional uncertainty yielding 2 at.% for concentrations higher than 10 at.%, 1 at.% when the concentration is between 10 at.% and 5 at.%, and 0.5 at.% for concentrations lower than 5 at.%.

Electrochemical testing. Electrochemical tests were performed in an argon filled glovebox in which the water and oxygen levels are kept below 1 ppm. A PTFE body is filled with electrolyte (1 M $LiClO_4$ in propylene carbonate (99.7%, Sigma-Aldrich)) and clamped against the working electrode. The base of the working electrode is a planar piece of a Si - 15 nm Ti - 150 nm PVD

TiN electrode stack that acts as a current collector and is cut to size. This current collector is then coated with the material of interest (e.g. a 29 nm as-deposited layer resulting from a 15 s TMP* - 15 s O_2* - 15 s $NiCp_2$ process), after which the electrode stack is clamped to the PTFE body with the with coated side pointing towards the electrolyte. The total surface area of the working electrode that is exposed to the liquid electrolyte is 1.05 cm^2. Li-strips (99.9%, Sigma-Aldrich) were used as both counter and reference electrodes. Measurements were carried out using either a home-built[29] or a commercial (Metrohm Autolab PGSTAT702) potentiostat/galvanostat.

Results and discussion

PE-ALD growth of nickel phosphate

For the growth of a nickel phosphate, the process developed by Dobbelaere et al.[21] for iron phosphate was altered. The process of Dobbelaere et al. relies on the plasma polymerisation behaviour of trimethyl phosphate (TMP), generating highly reactive plasma species at the substrate surface. At a substrate temperature below approximately 300°C, these phosphate esters showed to polymerise at the substrate surface leading to continuous growth of a phosphorus rich film. Only at sufficiently high substrate temperatures (300°C and higher), the polymerisation reactions become self-limited and saturated growth can take place. In these processes, the TMP* (with the star denoting a plasma) pulse is then typically followed by an oxygen plasma, which is used to combust the carbonaceous groups that are still attached to the chemisorbed TMP* species, and replace them with hydroxyl groups. Next, a metalorganic precursor is pulsed to incorporate the metal into the phosphate network. For the deposition of nickel phosphate in this work, nickelocene ($NiCp_2$) was chosen. Metalocenes have already proven to be suitable ALD precursors in the past, increasing the chances of nickelocene being a successful self-limiting precursor for the deposition of nickel phosphate. When pulsing multiple cycles of a 15 s TMP* - 10 s O_2 - 10 s $NiCp_2$ process at a substrate temperature of 300°C, substrate enhanced growth is then observed using in-situ ellipsometry

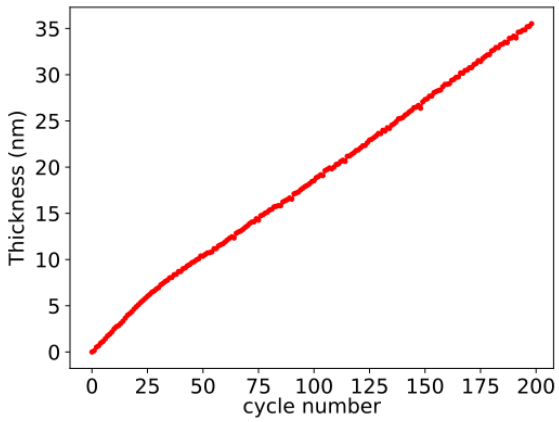

Figure 1: Increase in thickness with increasing cycle number in the TMP* - O_2* - $NiCp_2$ process, studied using in-situ ellipsometry.

(figure 1). This means that in the first cycles a growth rate of 0.24 nm/cycle is found, which then decreases to a stable 0.17 nm/cycle in the subsequent cycles. This type of growth has been reported in literature already, and indicates that the substrate surface contains more active sites for the precursor to react with than when it is fully covered by the deposited layer[30].

To study the self-limiting nature of the deposition process at this temperature, additional in-situ ellipsometry measurements were performed with varying precursor exposure times. In these depositions, the exposure time of one precursor was varied, while the two other precursor doses were kept constant. The constant exposure times were chosen to be 15 s

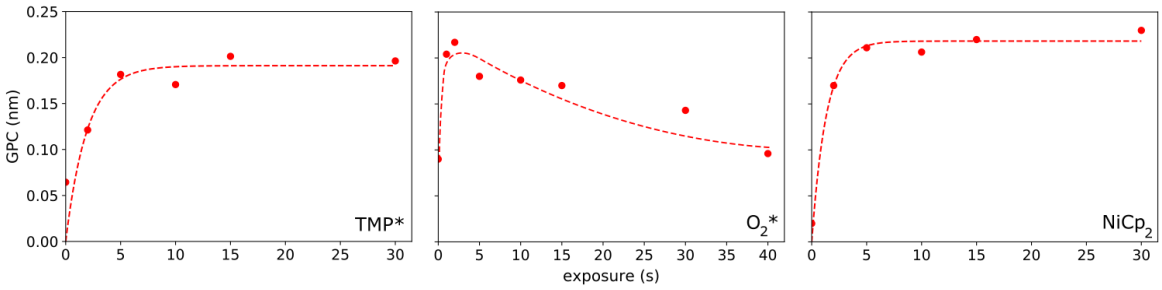

Figure 2: Saturation of TMP*, O_2* and $NiCp_2$ at a substrate temperature of 300 °C.

for TMP*, 15 s for O_2* and 10 s for $NiCp_2$. From the data in figure 2 it can be seen that saturation is observed for TMP* and $NiCp_2$, where a red dotted line is also shown indicating a fit of the shape (1-e^{-x}). For oxygen plasma, the growth per cycle (GPC) shows to increase at low exposure (which is thought to be due to removal of methoxy groups at the surface that remained after the TMP* pulse), and continuously decreases with further increasing exposure times. In this case, the red dotted line merely acts as a guide to the eye. The continuously decreasing GPC with increasing oxygen plasma exposure was also observed in PE-ALD of titanium phosphate[22], but the exact nature of the decrease is not yet clear. The main function of this process step is however to remove carbon contamination, which can be obtained after only a few seconds minimising the need for long and non-saturative pulses. If avoiding carbon contamination is not critical for a specific application, this step can even be left out completely. Nevertheless, an ALD like process is observed with self-limiting reactions for TMP* and $NiCp_2$, with an optimised growth rate of approximately (0.19 ± 0.01) nm/cycle.

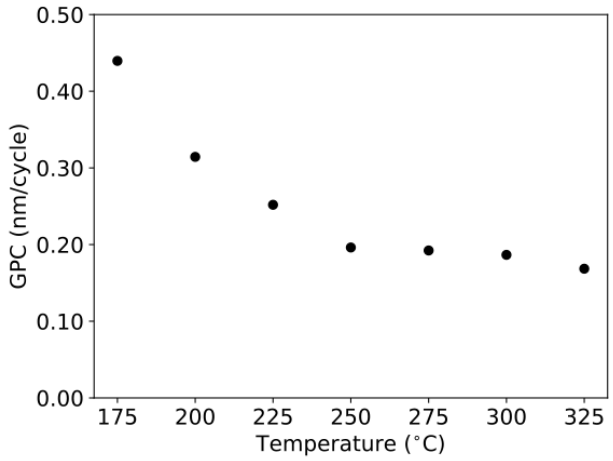

Figure 3: Temperature dependence of the growth rate when pulsing TMP*, O_2* and $NiCp_2$.

In measuring the temperature dependence of the growth per cycle (a 15 s TMP*, 15 s O_2*, 15 s $NiCp_2$ process), an increase of the GPC can be found with decreasing substrate temperature (figure 3). This is to be expected, as the polymerisation of TMP* has already

proven to result in continuous growth below a certain threshold temperature. Only when the substrate temperature is above this value, self-limiting reactions are expected, as was observed here near 300°C (figure 2).

Thin film characterisation

Thin film composition and chemical structure. To better understand the chemical composition and structure of the as-deposited layer, X-ray photoelectron spectroscopy (XPS) and elastic recoil detection (ERD) are used. The XPS spectra measured at the surface of an approximately 35 nm thick layer resulting from the TMP* - O_2* - $NiCp_2$ process are shown in figure 4. Only the spectrum of the surface is presented, as studying the bulk material through sputtering with Ar-ions was not possible due to damaging effects (shifting the nickel peak). Calibration was done using a 284.6 eV peak position for C-C bonds. For

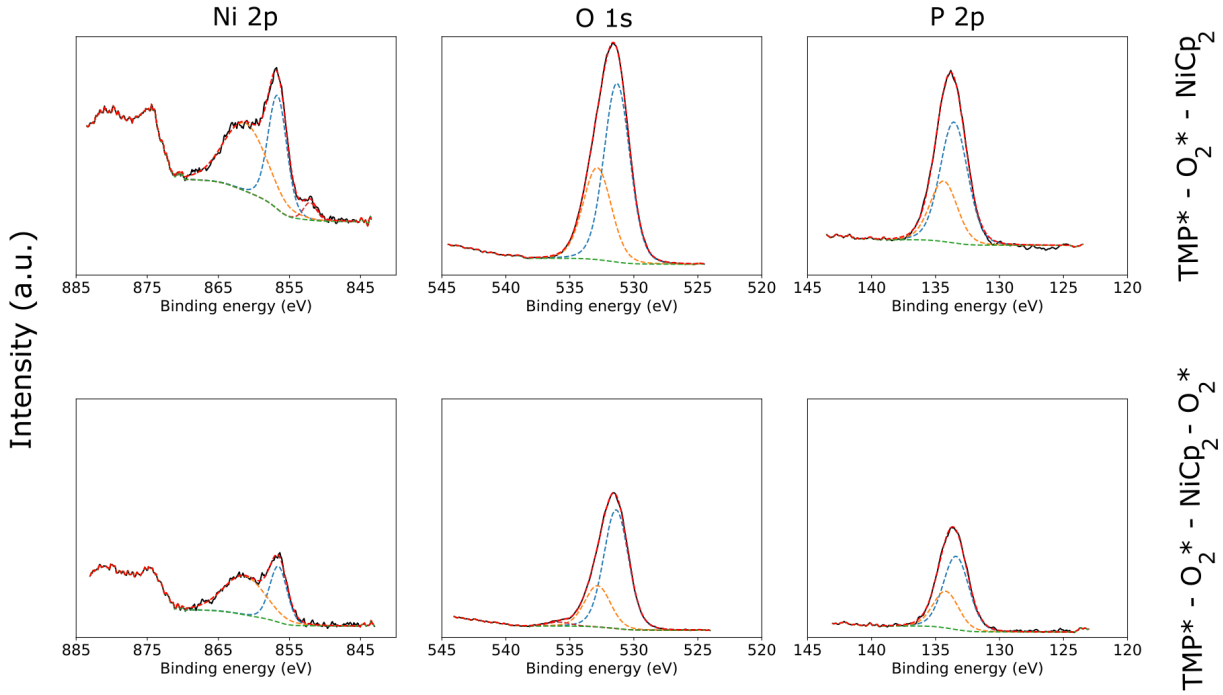

Figure 4: XPS spectra of Ni 2p, O 1s and P 2p at the surface of a thin film resulting from the TMP*-O_2*-$NiCp_2$ (top) and TMP*-O_2*-$NiCp_2$-O_2* (bottom) process. The peaks of one element are plotted at the same scale for both processes.

the Ni $2p_{3/2}$ peak, three components were observed. The largest contribution comes from a component at 856.7 eV, and is thought to be related to a 2+ oxidation state of nickel[31–33], with a satellite peak at 861.2 eV. A minor component is also observed at 852.1 eV, which is thought to be metallic nickel.[34,35] The origin of this component is unclear, but could be the result of precursor decomposition.[35] However, the component only adds a small contribution to the Ni 2p spectrum, and saturation of the nickel precursor was achieved suggesting that this is only a minor component. In the O 1s peak, two components are observed. The low binding energy component at 531.3 eV is characteristic for oxygen in a phosphate environment[18,21,36], while the component at 532.9 eV is characteristic for bridging oxygen (P-O-P)[37] that is formed during the TMP* pulse. The P 2p peak is split in a $2p_{3/2}$ component at 133.6 eV and a $2p_{1/2}$ component at 134.4 eV, which is also consistent with a phosphate-like environment[18,21,36].

As Ni^{3+} would be needed when aiming at high voltage Li-ion battery applications (if the phosphate is fully delithiated), we also explored an alternative process where an additional oxygen plasma was pulsed after the $NiCp_2$ step (i.e. TMP*-O_2*-$NiCp_2$-O_2*). However, very similar peak shapes and positions in XPS were observed with this altered process (figure 4, bottom). The only major difference is the disappearing of the Ni^0 contamination, which has been either completely removed or simply oxidised into Ni^{2+}. This means that, if the high voltage Ni^{3+}/Ni^{2+} couple is really needed, alternative processes would be required. One way to achieve this could for example be by depositing a (non lithiated) phosphate using a different nickel precursors with nickel in the Ni^{3+} oxidation state. A different approach could be to maintain nickel in a Ni^{2+} oxidation state, but also include a lithium precursor to lithiate the nickel phosphate during deposition. In that way, the Ni^{3+}/Ni^{2+} redox couple might still be observed by electrochemically delithiating the phosphate. These alternative processes were not investigated in this work, but the electrochemical activity of the layers deposited using the current ALD process will still be discussed later on in this manuscript.

As the compositional analysis resulting from XPS can have a large error, the study on the composition was done using ERD. From these measurements (table 1), a stoichiometry of approximately $Ni_3(P_{0.8}O_{3.1})_2$ and $Ni_3(P_{0.9}O_{3.7})_2$ is observed for layers deposited respectively with and without the additional oxygen plasma step. Both are relatively close to stoichiometric $Ni_3(PO_4)_2$, with the latter process getting closest to it. Such an increase in nickel to phosphate ratio with the incorporation of an additional oxygen plasma has been observed in literature before, and is though to be due to the reaction with the adsorbed metalorganic molecules at the surface, optimising the reactivity towards the subsequent TMP (plasma) pulse.[38] It is also interesting to note that the phosphorus-to-metal ratio (P/M) of approximately 0.5 is much lower than what is observed for most phosphates deposited using a TMP*. Only the P/M ratio of vanadium phosphate (0.9) is lower than one, while most other phosphates have a ratio around 1.5 or higher. There is so far no clear reason why vanadium and nickel phosphate have a lower P/M ratio than most other phosphates, and this would require a more in-depth analysis. However, as the goal of this work is primarily to report the initial growth possibilities, such an analysis was not performed here.

Table 1: Atomic concentrations of nickel phosphate with and without an additional oxygen plasma step, measured with ERD.

Deposition process	**C (at.%)**	**Ni (at.%)**	**P (at.%)**	**O (at.%)**	**H (at.%)**
TMP*-O_2*-$NiCp_2$	1.2	25	13.6	50.1	10.2
TMP*-O_2*-$NiCp_2$-O_2*	0.3	22.0	13.7	54.2	8.9

From the compositional analysis it is also clear that the carbon level in the thin film is relatively low for both processes, with the process with the additional oxygen plasma step having the lowest amount of carbon. The decrease in carbon content with the addition of an extra oxygen plasma step means that the oxygen plasma can very efficiently remove the Cp-ligands of nickelocene, presumably through a combustion-like reaction.[39] Hydrogen was also detected, which could originate from un-reacted ligands from the nickel precursor, the

combustion of these ligands during the deposition process and/or water that was absorbed from the air.

Thin film crystallinity. From XRD measurements, the amorphous nature of the as-deposited film resulting from the TMP*-O_2*-$NiCp_2$ process was observed. However, after annealing (at a rate of 5°C/min) the sample in various atmospheres, crystalline structures could be obtained. When annealing the nickel phosphate in a H_2 atmosphere to 950°C, crystalline Ni_2P is clearly formed. It does have to be noted that phosphine gas (PH_3) might be formed during this anneal, which can become a safety concern. However, for the thin films in this work (with a low amount of material undergoing the annealing process), the amount of gas that is produced is expected to be rather low.[26] For an anneal in He, peaks that can be related to crystalline $Ni_3(PO_4)_2$ appear in the spectrum. SEM and AFM analysis before and after anneal into both crystalline phases is presented in the supporting information. Interestingly, in the process where an additional oxygen plasma is pulsed after nickelocene (i.e. TMP*-O_2*-$NiCp_2$-O_2*), two peaks at approximately 26° and 32.5° are observed in the spectrum of the as-deposited layer (figure S2). These peaks remain present after anneal in helium atmosphere and might be linked to crystalline $Ni_3(PO_4)_2$.[40] Apart from these two

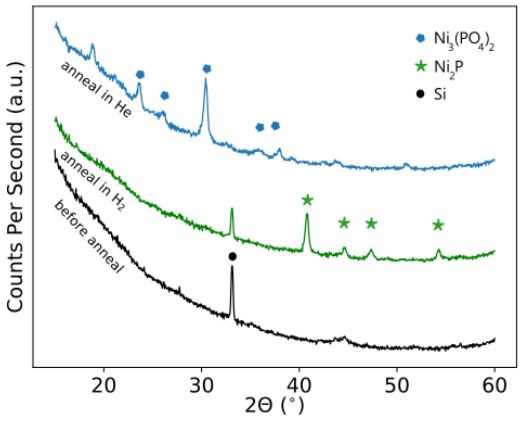

Figure 5: XRD spectrum of as deposited nickel phosphate (from the TMP* - O_2* - $NiCp_2$ process) compared to the spectra after anneal in various atmospheres.

peaks, additional peaks appear upon annealing in helium, resulting in a diffraction pattern similar to the one in figure 5. This shows that the addition of an oxygen plasma after the nickelocene step not only results in a composition closer to stoichiometric $Ni_3(PO_4)_2$, but seems to induce some crystallinity in the as deposited layer (which can be further improved by annealing in a helium atmosphere).

PE-ALD phosphates as LIB electrodes

The nickel phosphate that is deposited by the novel process in this work (i.e. the as-deposited layer resulting from a 15 s TMP* - 15 s O_2* - 15 s $NiCp_2$ process) will now be electrochemically characterised and compared to cobalt and iron phosphate. For the deposition of iron phosphate, a process similar to the one discussed above, but using tert-butylferrocene (TBF) instead of nickelocene, has already been shown to result in electrochemically active iron phosphate deposited through PE-ALD.[25] Similarly, a deposition process for cobalt phosphate has also already developed earlier[26], but its potential use as an LIB electrode was not yet characterised.

For iron phosphate it has been shown that an activation at low potential vs. Li^+/Li is needed for the material to become electrochemically active (figure 6). This sharp peak was suggested to originate from the formation of metallic iron and lithium phosphate, which could then be re-oxidised into $FePO_4$ by delithiating the electrode. Upon subsequent cycles, a stable Fe^{2+}/Fe^{3+} redox system was observed. In this work, cobalt and nickel phosphate (deposited using the TMP*-O_2*-metalocene process) show similar activation behaviour in their cyclic voltammogram, although with an activation at a different potential (figure 6). Focussing on nickel phosphate in particular, such activation at low potential has even been observed in literature for an $Ni_3(PO_4)_2$ LIB electrode.[41,42] For this material, the activation peak at low potential was thought to be a conversion reaction (similar to iron phosphate), reducing Ni^{2+} to metallic nickel. Such reaction is verified here by comparing the charge that is expected

for the reaction (using Faraday's law) with the capacity associated with the cathodic activation in this work.[25] Theoretically, a capacity of 4.8 μAhcm^{-2} is expected from the exchange of 2 electrons (i.e. reducing Ni^{2+} to metallic nickel). In this work, a total capacity of 5.7 μAhcm^{-2} (associated with the activation peak) is however observed, meaning approximately 2.4 electrons are exchanged per nickel atom (see supporting information). Based on these findings, and the agreement with previous reports, the activation of PE-ALD grown nickel phosphate is thus thought to be governed by the following reaction:

$$Ni_3(PO_4)_2 + 6Li^+ + 6e^- \rightarrow 3Ni + 2Li_3PO_4 + SEI \tag{1}$$

The observed excess charge (i.e. a charge of 4.8 μAhcm^{-2} was expected theoretically, while a charge of approximately 5.7 μAhcm^{-2} was observed) is then thought to originate from the formation of a solid electrolyte interface (SEI) in the first cycle.[3,25] For cobalt phosphate, no compositional analysis of the layer using ERD was available, meaning a direct validation of the reaction mechanism was not possible. However, by assuming that the stoichiometry of the deposited layer is identical to what was observed by Rongé et al. ($CoP_{2.3}O_{6.7}$)[26], an

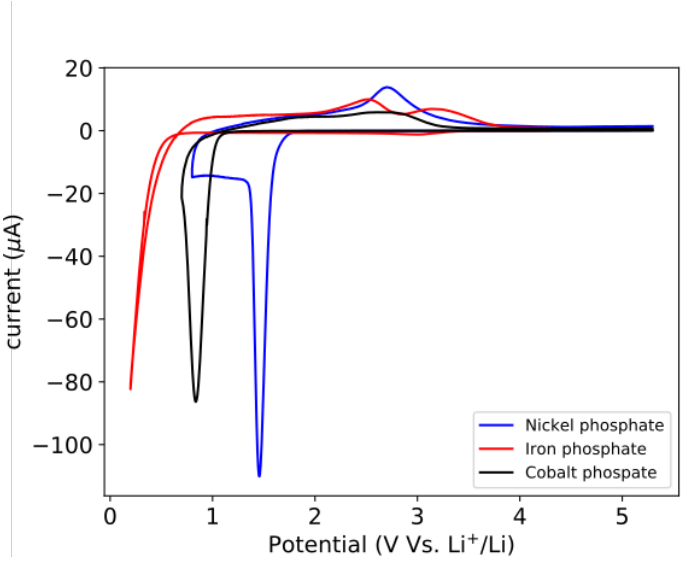

Figure 6: Initial cycle of a 33 nm iron (red), 28 nm cobalt (black) and 29 nm nickel (blue) phosphate thin film, showing an activation at low potential during the first cathodic scan. The scan rate is 1 mv/s.

initial idea about the reaction mechanism was formed in the supporting information. Based on these assumptions, a reaction similar to the nickel phosphate layer is expected, leaving behind metallic Co in a lithium phosphate matrix.

After this activation step, electrochemical activity is observed for all phosphates in a potential window between 1.3 - 4 V vs. Li^+/Li. No activity was observed at higher potentials for cobalt and nickel phosphate, which is thought to originate from the oxidation state of the metal in both phosphates (as mentioned earlier). To obtain for example the high voltage Ni^{2+}/Ni^{3+} redox couple, a delithiated nickel phosphate with Ni^{3+} would be needed. As this is not the case, the high voltage electrochemical reaction can thus not be observed. The introduction of an additional oxygen plasma in the PE-ALD process also did not change the cyclic voltammogram significantly (figure S3), further proving that the oxygen plasma did not dramatically change the nature of the phosphate, as expected from the earlier thin film characterisation. A similar explanation is expected for the absence of a high voltage redox couple in cobalt phosphate, since the nature of both nickel and cobalt precursor (with the metal already in the 2+ oxidation state[26]) is very similar. A change in metal precursor might thus be needed (with the metal built in with a 3+ oxidation state) to achieve the redox couple at high potential.

Nevertheless, both phosphates do show reversible electrochemical activity after the activation at low potential (figure 7), meaning they can still be characterised (and compared to iron phosphate) as an LIB electrode. Both nickel and cobalt phosphate show to operate at a lower potential than iron phosphate, but with a higher specific capacity. The nature of the reversible redox couple appearing after initial activation is however not fully clear. In the first few cycles after activation of the nickel phosphate, the cathodic activation peak shifts to higher potential and decreases in magnitude. It consists of 2 overlapping peaks, with the peak at higher voltage slowly disappearing in the subsequent cycles (figure S4). The

anodic peak however remains at the same position and maintains the same peak shape. In the work of Aziam et al., the anodic peak following activation is thought to be related to re-oxidising the nickel to Ni^{2+}, completing the reversible conversion reaction. Such electron (or lithium) transfer would be in line with the observed charge of 4.1 μAh/cm^2 related to this peak, as the transfer of two electrons (or lithium ions) should result in an expected charge of approximately 4.8 μAh/cm^2 (supporting information). A different reaction mechanism is proposed by Li et al.,[42] where the redox couple is though to originate from an alloying

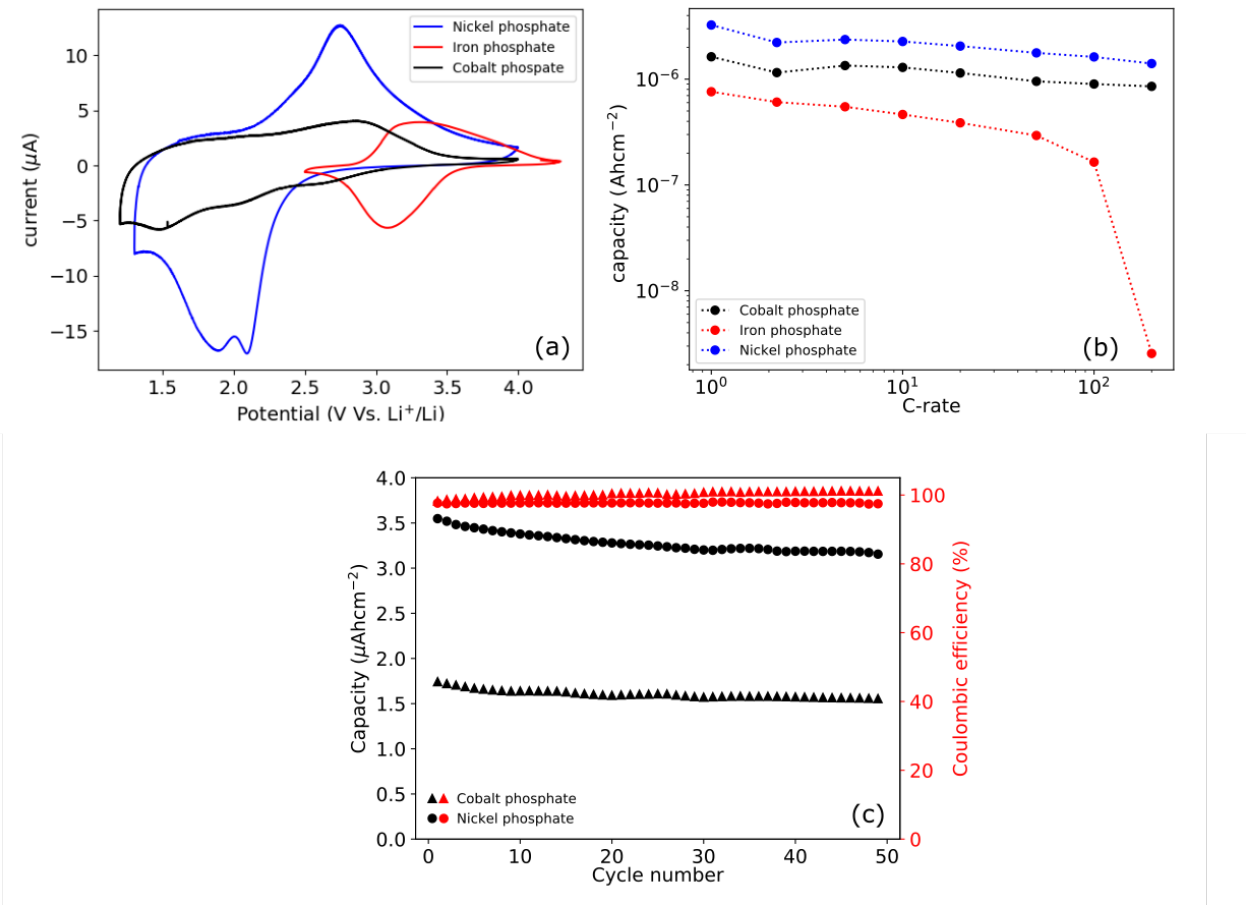

Figure 7: (a) Cyclic voltammogram of iron, cobalt and nickel phosphate after initial electrochemical activation, measured with a scan rate of 1 mv/s. (b) Rate capabilities during charging various phosphates highlighting the good rate behavior of both cobalt and nickel phosphate. (c) Capacity (black) and coulombic efficiency (red) of nickel and cobalt phosphate during 50 cycles. For the cycle life of iron phosphate we refer to the work of Dobbelaere et al.[25]

reaction between lithium and nickel. This is close to what has also been observed for other metal phosphates[19,43], and is based on the fact that the metallic nickel is dispersed in the lithium phosphate matrix, making it a relatively stable structure over the course over multiple cycles of alloying. Although the exact reaction mechanism was not further studied in this work, it is clear that the high capacity that is obtained with respect to iron phosphate (approximately 1172 mAh/cm^3 for nickel phosphate when the layer thickness is taken into account, with respect to 228 mAh/cm^3 for iron phosphate in this work) does agree with one of such reaction paths as these typically allow for higher capacities than intercalation reactions (such as the reaction mechanism in iron phosphate). For cobalt phosphate, a similar reaction mechanism is again expected (see supporting), with the reversible redox couple again being either the continuation of the conversion reaction present during activation, or a complex alloying process, leading to a fairly high specific capacity of approximately 571 mAh/cm^3 with respect to the capacity of iron phosphate.

Apart from a higher overall capacity, nickel and cobalt phosphate also show better rate capability over iron phosphate (figure 7(b)), showing that both materials do have some interesting properties for LIB applications. The cycle life and coulombic efficiency of both nickel and cobalt phosphate are also presented in figure 7(c). Both materials exhibit a good coulombic efficiency with a decent, but not ideal, cycle life (where approximately 89% of the capacity is retained after 50 cycles for both phosphates). The capacity retention is slightly worse compared to other metal phosphates deposited through a similar ALD process[22,23,25], which is thought to originate from the nature of the electrochemical reactions. While the previously reported metal phosphates relied on intercalation-type reactions, the conversion or alloying reactions that might take place in the nickel and cobalt phosphate could lead to a slightly less stable cycle life.

Although both phosphates do have some interesting properties for LIB applications, they

would ideally operate at a higher potential. The low operating potential for example means that the energy will be rather low when using the materials as a LIB cathode, or that the material would stay permanently delithiated when using it as a coating on e.g. an lithium nickel manganese cobalt oxide (NMC) electrode. Although it is interesting to understand the working of the current layers, it would thus also be of interest to further look into the synthesis of these layers in an attempt to e.g. enhance the operating voltage.

Conclusion

Nickel phosphate was deposited by subsequently pulsing a TMP plasma, an oxygen plasma and nickelocene at a substrate temperature of 300°C. Saturation was observed for both TMP* and $NiCp_2$ at a GPC of approximately 0.2 nm/cycle (with an oxygen plasma pulse of 15 s), using in-situ ellipsometry. A decreasing GPC with increasing oxygen plasma pulse time was observed, but the pulse time can be kept relatively short as the main function of this process step is to remove carbon contamination. The composition of the as-deposited layer as measured by ERD indicates a stoichiometry of approximately $Ni_3(P_{0.8}O_{3.1})_2$ which is close to stoichiometric $Ni_3(PO_4)_2$. If an additional oxygen plasma is pulsed after the nickelocene step, the composition is observed to resemble this material even closer, with a stoichiometry of $Ni_3(P_{0.9}O_{3.7})_2$. Using XPS, nickel was observed to be mainly in the Ni^{2+} oxidation state, with and without the additional oxygen plasma. The as-deposited layer resulting from the process without the additional oxygen plasma showed to be amorphous, but could be crystallised to either $Ni_3(PO_4)_2$ or Ni_2P through an anneal in respectively a helium and hydrogen atmosphere. The layer resulting from the process with the additional oxygen plasma already showed small peaks indicating crystalline $Ni_3(PO_4)_2$ before anneal, but could be further crystallised through annealing in helium. PE-ALD deposited cobalt and nickel phosphate were then electrochemically characterised for the first time, revealing the need for electrochemical activation at low potential, similar to previously reported iron

phosphate. After this activation, reversible electrochemical behaviour is observed for both phosphates around approximately 2.5 V vs Li^+/Li. No peak was observed at higher potential, indicating that the Ni^{3+}/Ni^{2+} or Co^{3+}/Co^{2+} redox couples could not be obtained with the proposed ALD processes. Nevertheless, a high capacity with excellent rate behaviour was observed for both phosphates (resulting from either a conversion or alloying reaction).

References

(1) Zhao, H.; Yuan, Z.-Y. Insights into transition metal phosphate materials for efficient electrocatalysis. *ChemCatChem* **2020**, *12*, 3797–3810.

(2) Masquelier, C.; Croguennec, L. Polyanionic (phosphates, silicates, sulfates) frameworks as electrode materials for rechargeable Li (or Na) batteries. *Chemical Reviews* **2013**, *113*, 6552–6591.

(3) Verma, P.; Maire, P.; Novák, P. A review of the features and analyses of the solid electrolyte interphase in Li-ion batteries. *Electrochimica Acta* **2010**, *55*, 6332–6341.

(4) Fang, Y.; Zhang, J.; Xiao, L.; Ai, X.; Cao, Y.; Yang, H. Phosphate framework electrode materials for sodium ion batteries. *Advanced Science* **2017**, *4*, 1600392.

(5) Ceder, G. Opportunities and challenges for first-principles materials design and applications to Li battery materials. *MRS bulletin* **2010**, *35*, 693–701.

(6) Ong, S. P.; Chevrier, V. L.; Hautier, G.; Jain, A.; Moore, C.; Kim, S.; Ma, X.; Ceder, G. Voltage, stability and diffusion barrier differences between sodium-ion and lithium-ion intercalation materials. *Energy & Environmental Science* **2011**, *4*, 3680–3688.

(7) Herle, P. S.; Ellis, B.; Coombs, N.; Nazar, L. Nano-network electronic conduction in iron and nickel olivine phosphates. *Nature materials* **2004**, *3*, 147–152.

(8) Karthickprabhu, S.; Vikraman, D.; Kathalingam, A.; Prasanna, K.; Kim, H.-S.; Karuppasamy, K. Electrochemical and cycling performance of neodymium (Nd^{3+}) doped $LiNiPO_4$ cathode materials for high voltage lithium-ion batteries. *Materials Letters* **2019**, *237*, 224–227.

(9) Fisher, C. A.; Hart Prieto, V. M.; Islam, M. S. Lithium battery materials Li M PO_4 (M= Mn, Fe, Co, and Ni): insights into defect association, transport mechanisms, and doping behavior. *Chemistry of Materials* **2008**, *20*, 5907–5915.

(10) Örnek, A. Influences of different reaction mediums on the properties of high-voltage $LiNiPO_4$@ C cathode material in terms of dielectric heating efficiency. *Electrochimica Acta* **2017**, *258*, 524–534.

(11) Shi, Y.; Zhang, M.; Qian, D.; Meng, Y. S. Ultrathin Al2O3 coatings for improved cycling performance and thermal stability of LiNi0. 5Co0. 2Mn0. 3O2 cathode material. *Electrochimica Acta* **2016**, *203*, 154–161.

(12) Mattelaer, F.; Vereecken, P. M.; Dendooven, J.; Detavernier, C. The influence of ultrathin amorphous ALD alumina and Titania on the rate capability of anatase TiO2 and LiMn2O4 Lithium ion battery electrodes. *Advanced Materials Interfaces* **2017**, *4*, 1601237.

(13) Johnson, R. W.; Hultqvist, A.; Bent, S. F. A brief review of atomic layer deposition: from fundamentals to applications. *Materials today* **2014**, *17*, 236–246.

(14) Meng, X.; Yang, X.-Q.; Sun, X. Emerging applications of atomic layer deposition for lithium-ion battery studies. *Advanced Materials* **2012**, *24*, 3589–3615.

(15) Liu, J.; Sun, X. Elegant design of electrode and electrode/electrolyte interface in lithium-ion batteries by atomic layer deposition. *Nanotechnology* **2014**, *26*, 024001.

(16) Li, W.; Song, Q.; Li, M.; Yuan, Y.; Zhang, J.; Wang, N.; Yang, Z.; Huang, J.; Lu, J.; Li, X. Chemical Heterointerface Engineering on Hybrid Electrode Materials for Electrochemical Energy Storage. *Small Methods* **2021**, 2100444.

(17) Wu, K.; Li, W.; Qin, J.; Hao, Y.; Sari, H. M. K.; Feng, H.; Li, X. Controllable atomic layer deposition coatings to boost the performance of $LiMn_xCoyNi_{1-x-y}O_2$ in lithium-ion batteries: A review. *Journal of Materials Research* **2020**, *35*, 762–774.

(18) Henderick, L.; Hamed, H.; Mattelaer, F.; Minjauw, M.; Nisula, M.; Meersschaut, J.; Dendooven, J.; Safari, M.; Vereecken, P.; Detavernier, C. Plasma enhanced atomic layer deposition of a (nitrogen doped) Ti phosphate coating for improved energy storage in Li-ion batteries. *Journal of Power Sources* **2021**, *497*, 229866.

(19) Xiao, Y.; Lee, J.; Yu, A.; Liu, Z. Electrochemical Performance of Amorphous and Crystalline $Sn_2P_2O_7$ Anodes in Secondary Lithium Batteries. *Journal of the Electrochemical Society* **1999**, *146*, 3623.

(20) Henderick, L.; Hamed, H.; Mattelaer, F.; Minjauw, M.; Meersschaut, J.; Dendooven, J.; Safari, M.; Vereecken, P.; Detavernier, C. Atomic Layer Deposition of Nitrogen-Doped Al Phosphate Coatings for Li-Ion Battery Applications. *ACS applied materials & interfaces* **2020**, *12*, 25949–25960.

(21) Dobbelaere, T.; Roy, A. K.; Vereecken, P.; Detavernier, C. Atomic layer deposition of aluminum phosphate based on the plasma polymerization of trimethyl phosphate. *Chemistry of Materials* **2014**, *26*, 6863–6871.

(22) Dobbelaere, T.; Mattelaer, F.; Roy, A. K.; Vereecken, P.; Detavernier, C. Plasma-enhanced atomic layer deposition of titanium phosphate as an electrode for lithium-ion batteries. *Journal of Materials Chemistry A* **2017**, *5*, 330–338.

(23) Dobbelaere, T.; Mattelaer, F.; Vereecken, P. M.; Detavernier, C. Plasma-enhanced atomic layer deposition of vanadium phosphate as a lithium-ion battery electrode ma-

terial. *Journal of Vacuum Science & Technology A: Vacuum, Surfaces, and Films* **2017**, *35*, 041513.

(24) Dobbelaere, T.; Minjauw, M.; Ahmad, T.; Vereecken, P.; Detavernier, C. Plasma-enhanced atomic layer deposition of zinc phosphate. *Journal of Non-Crystalline Solids* **2016**, *444*, 43–48.

(25) Dobbelaere, T.; Mattelaer, F.; Dendooven, J.; Vereecken, P.; Detavernier, C. Plasma-enhanced atomic layer deposition of iron phosphate as a positive electrode for 3D lithium-ion microbatteries. *Chemistry of Materials* **2016**, *28*, 3435–3445.

(26) Rongé, J.; Dobbelaere, T.; Henderick, L.; Minjauw, M. M.; Sree, S. P.; Dendooven, J.; Martens, J. A.; Detavernier, C. Bifunctional earth-abundant phosphate/phosphide catalysts prepared via atomic layer deposition for electrocatalytic water splitting. *Nanoscale Advances* **2019**, *1*, 4166–4172.

(27) Xie, L.-Y.; Xiao, D.-Q.; Pei, J.-X.; Huo, J.; Wu, X.; Liu, W.-J.; Ding, S.-J. Growth, physical and electrical characterization of nickel oxide thin films prepared by plasma-enhanced atomic layer deposition using nickelocene and oxygen precursors. *Materials Research Express* **2020**, *7*, 046401.

(28) Meersschaut, J.; Vandervorst, W. High-throughput ion beam analysis at imec. *Nuclear Instruments and Methods in Physics Research Section B: Beam Interactions with Materials and Atoms* **2017**, *406*, 25–29.

(29) Dobbelaere, T.; Vereecken, P. M.; Detavernier, C. A USB-controlled potentiostat/galvanostat for thin-film battery characterization. *HardwareX* **2017**, *2*, 34–49.

(30) Puurunen, R. L. Surface chemistry of atomic layer deposition: A case study for the trimethylaluminum/water process. *Journal of applied physics* **2005**, *97*, 9.

(31) Yang, D.; Yu, Q.; Gao, L.; Mao, L.; Yang, J.-H. The additive effect of graphene in nickel phosphate/graphene composite and enhanced activity for electrochemical oxidation of methanol. *Applied Surface Science* **2017**, *416*, 503–510.

(32) Surendran, S.; Sivanantham, A.; Shanmugam, S.; Sim, U.; Selvan, R. K. $Ni_2P_2O_7$ microsheets as efficient Bi-functional electrocatalysts for water splitting application. *Sustainable Energy & Fuels* **2019**, *3*, 2435–2446.

(33) Fa, D.; Yu, B.; Miao, Y. Synthesis of ultra-long nanowires of nickel phosphate by a template-free hydrothermal method for electrocatalytic oxidation of glucose. *Colloids and Surfaces A: Physicochemical and Engineering Aspects* **2019**, *564*, 31–38.

(34) Hengne, A. M.; Samal, A. K.; Enakonda, L. R.; Harb, M.; Gevers, L. E.; Anjum, D. H.; Hedhili, M. N.; Saih, Y.; Huang, K.-W.; Basset, J.-M. Ni–Sn-supported ZrO_2 catalysts modified by indium for selective CO_2 hydrogenation to methanol. *ACS omega* **2018**, *3*, 3688–3701.

(35) Pugmire, D.; Woodbridge, C.; Boag, N.; Langell, M. Adsorption and decomposition of nickelocene on Ag (1 0 0): a high-resolution electron energy loss spectroscopy and temperature programmed desorption study. *Surface science* **2001**, *472*, 155–171.

(36) Zhan, Y.; Lu, M.; Yang, S.; Liu, Z.; Lee, J. Y. The origin of catalytic activity of nickel phosphate for oxygen evolution in alkaline solution and its further enhancement by iron substitution. *ChemElectroChem* **2016**, *3*, 615–621.

(37) Kozen, A. C.; Pearse, A. J.; Lin, C.-F.; Noked, M.; Rubloff, G. W. Atomic layer deposition of the solid electrolyte LiPON. *Chemistry of Materials* **2015**, *27*, 5324–5331.

(38) Hornsveld, N.; Kessels, W.; Creatore, M. Atomic Layer Deposition of Aluminum Phosphate Using $AlMe_3$, $PO(OMe)_3$, and O_2 Plasma: Film Growth and Surface Reactions. *The Journal of Physical Chemistry C* **2020**, *124*, 5495–5505.

(39) Di Palma, V.; Knoops, H. C.; Kessels, W. M.; Creatore, M. Atomic layer deposition of cobalt phosphate from cobaltocene, trimethylphosphate, and O_2 plasma. *Journal of Vacuum Science & Technology A: Vacuum, Surfaces, and Films* **2020**, *38*, 022416.

(40) Omar, F. S.; Numan, A.; Duraisamy, N.; Bashir, S.; Ramesh, K.; Ramesh, S. Ultrahigh capacitance of amorphous nickel phosphate for asymmetric supercapacitor applications. *RSC advances* **2016**, *6*, 76298–76306.

(41) Aziam, H.; Indris, S.; Knapp, M.; Ehrenberg, H.; Saadoune, I. Synthesis, Characterization, Electrochemistry, and In Situ X-ray Diffraction Investigation of $Ni_3(PO_4)_2$ as a Negative Electrode Material for Lithium-Ion Batteries. *ChemElectroChem* **2020**, *7*, 3866–3873.

(42) Li, T.; Cai, R.; Nie, X.; Tjong, J. Porous $Ni_3(PO_4)_2$ thin film as a binder-free and low-cost anode of a high-capacity lithium-ion battery. *Journal of Electroanalytical Chemistry* **2019**, *835*, 81–85.

(43) Liu, Z.; Lee, J. Y. Electrochemical performance of $Pb_3(PO_4)_2$ anodes in rechargeable lithium batteries. *Journal of power sources* **2001**, *97*, 247–250.

Supporting information

Supporting information is available containing (1) additional XRD data, (2) calculations towards validation of the electrochemical reactions, (3) additional cyclic voltammetry data.

Keywords

Nickel, cobalt, metal phosphate, Li ion, batteries, Atomic Layer Deposition

Acknowledgements

The authors are grateful for financial support to FWO-Vlaanderen and the Special Research Fund BOF of Ghent University (GOA project, Grant No. 01G01019, and SBO XL-Lion, S005017N). M. M. and J.D. acknowledge FWO-Vlaanderen for a post-doctoral fellowship. The authors would also like to thank Olivier Janssens for conducting the SEM measurments.

Conflicts of interest

There are no conflicts of interest to declare.

TOC image

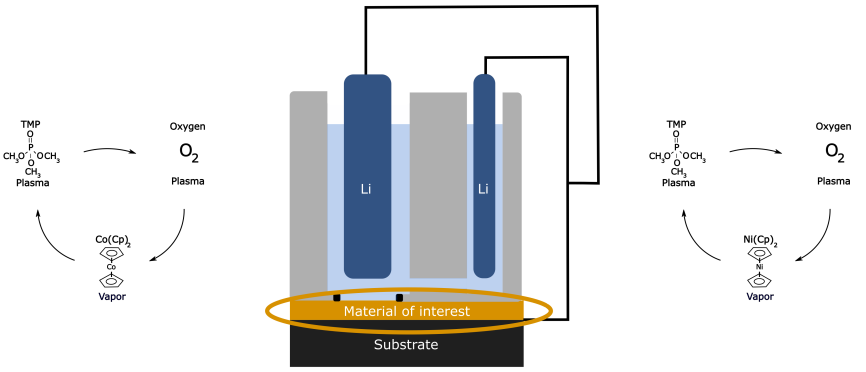

Cobalt phosphate and nickel phosphate

for LIB applications

Supporting information to 'Plasma Enhanced Atomic Layer Deposition of Nickel and Cobalt Phosphate for Lithium Ion Batteries'

Lowie Henderick,[†] Ruben Blomme,[†] Matthias Minjauw,[†] Jonas Keukelier,[†] Johan Meersschaut,[‡] Jolien Dendooven,[†] Philippe Vereecken,[‡] and Christophe Detavernier*[,†]

†*Department of Solid State Sciences, Ghent University, Krijgslaan 281 S1, 9000 Gent, Belgium*

‡*imec, Kapeldreef 75, B-3001 Heverlee, Belgium*

E-mail: Christophe.Detavernier@Ugent.be

Deposition of nickel phosphate

To complete the thin film characterisation, the surface morphology before and after an anneal into a crystalline phase was studied using SEM (figure S1(a,b,c)). The as-deposited, amorphous, layer showed to be a closed and relatively smooth film. The crystallisation into $Ni_3(PO_4)_2$ clearly increased the roughness of the layer, with the material agglomerating into irregularly shapes islands. This is also observed after crystallisation into Ni_2P, although the agglomerates are more spherical, smaller and more densely packed. The same conclusion can be drawn from AFM measurements, as can be seen in figure S1(d,e,f). The roughness clearly increased after annealing, going from a root mean square of 1.6 nm to 4.6 nm with the crystallisation into $Ni_3(PO_4)_2$ and 7.2 nm after crystallisation into Ni_2P.

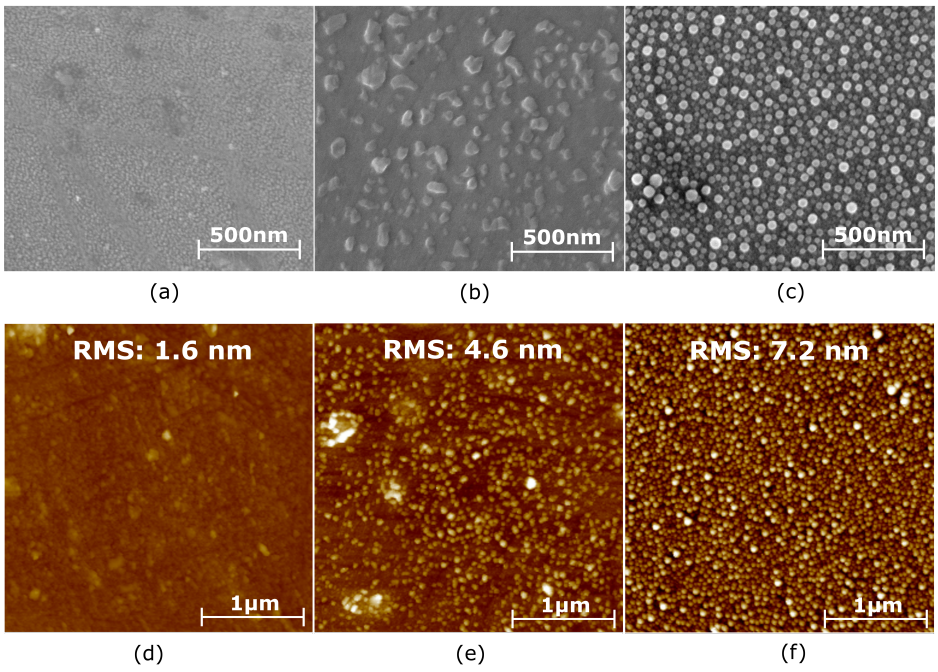

Figure S1: SEM and AFM images of the (a,d) as-deposited nickel phosphate, (b,e) after crystallisation into $Ni_3(PO_4)_2$ and (c,f) after crystallisation into Ni_2P. The root mean square of each AFM measurement is also presented, and the same color scale has been used for the three different samples.

The XRD diffraction pattern of nickel phosphate resulting from a TMP* - O_2* - $NiCp_2$ - O_2* process before and after anneal was also measured and is shown in figure S2. Two peaks (highlighted by the black arrows) are observed in the as deposited diffraction pattern, indicating that (to some degree) crystalline $Ni_3(PO_4)_2$ might have been formed during deposition. Only an anneal in helium and oxygen atmosphere was attempted, as the main goal was to see if the nickel could be further oxidised during the anneal. However, no clear changes were observed during the anneal in oxygen atmosphere while additional $Ni_3(PO_4)_2$ peaks are present after anneal in helium.

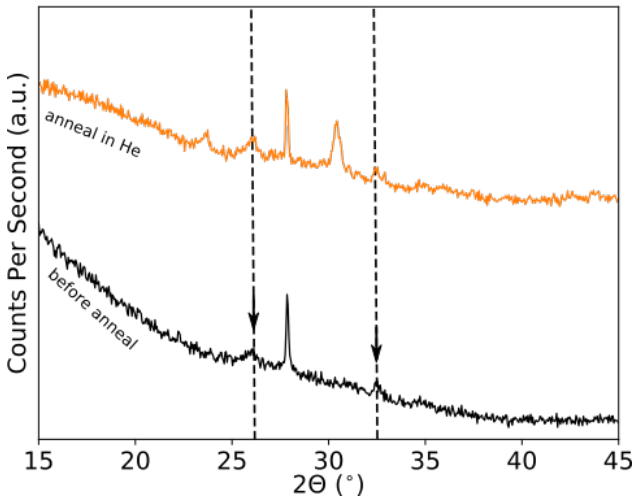

Figure S2: XRD diffraction pattern of as deposited nickel phosphate from the TMP* - O_2* - $NiCp_2$ - O_2* process, compared to the diffraction pattern after anneal in helium and oxygen. The black arrows denote peaks that can indicate a degree of crystallisation during the PE-ALD process.

PE-ALD phosphates as LIB electrodes

Reaction mechanism. To study the nature of the electrochemical activation of nickel phosphate, the observed charge of the activation peak can be compared to the expected charge for a particular reaction (similar to what was done for PE-ALD iron phosphate in

the work of Dobbelaere et al.). The latter can be calculated using Faraday's law:

$$\frac{Q}{A} = \frac{ndeρN_A}{M}$$

with $\frac{Q}{A}$ the charge per surface area, e the elementary charge, N_A is Avogadro's constant, n is the number of electrons transferred in the redox reaction, ρ is the density of the film, d is the thickness of the film and M is the molar mass. From the ERD composition, the molar mass of one $NiP_{0.5}O_2$ unit (normalised on nickel, to calculate the amount of electrons transferred per nickel atom) is 107 g/mol. The thickness and density (measured by XRR) were respectively 28 nm and 3.5 g/cm^3. This results in $\frac{Q}{A} = 2.4 * n$ μAh/cm^2, with the measured charge of the activation peak being equal to approximately 5.7 μAh/cm^2. A total of approximately 2.4 electrons (or lithium ions) per nickel atom have thus been transferred during activation. This seems to point towards a conversion reaction from Ni^{2+} to Ni^0 (a total of 2 electrons exchanged, with an expected charge of 4.8 μAh/cm^2), but with an excess charge (the remaining 0.9 μAh/cm^2 that was unaccounted for with respect to the measured charge) that can be attributed to the formation of a solid electrolyte interface (SEI).
The peak in the following anodic scan shows a capacity of 4.1 μAh/cm^2, or a total of 1.7 electrons (or lithium ions) transferred per nickel atom. This could be in line with the reversible conversion reaction (Ni^{2+}/Ni^0) of the nickel phosphate, or alternatively with a (de-)alloying process that involves the exchange of approximately 1.7 lithium ions per nickel atom. A coulombic efficiency close to 100% was then observed in the following cycles, indicating a reversible charge/discharge redox couple.

For the analysis of cobalt phosphate, a reliable compositional ERD analysis of the deposited layer would be needed. As this was not done in this work, only an assumption on the reaction mechanism can be made. Assuming a stoichiometry of $CoP_{2.3}O_{6.7}$, the molar mass of one unit would be 237 g/mol. The film thickness and density are 28 nm and approximately 3.2

g/cm^3 (measured with XRR). This results in $\frac{Q}{A} = 1 * n$ μAh/cm^2. An activation in which Co^{2+} is thus reduced to metallic cobalt would result in a charge of 2 μAh/cm^2. The measured charge during the activation of this cobalt phosphate is 4.1 μAh/cm^2. This could again be in line with the conversion reaction, with the formation of an SEI layer resulting in excess charge. In the following anodic scan, a charge of 2.1 μAh/cm^2 is observed. This would also agree with 2 electrons being transferred per cobalt atom, indicating a similar reaction path as for the nickel phosphate.

Cyclic voltammetry of nickel phosphate. For completion of the cyclic voltammetry study of the PE-ALD nickel phosphate, the comparison between layers deposited with the TMP* - O_2* - $NiCp_2$ - O_2* process and the TMP* - O_2* - $NiCp_2$ process is presented in figure S3. Here it is observed that the shape of the voltammograms is very similar, meaning the additional oxygen plasma did not dramatically change the electrochemical nature of the phosphate.

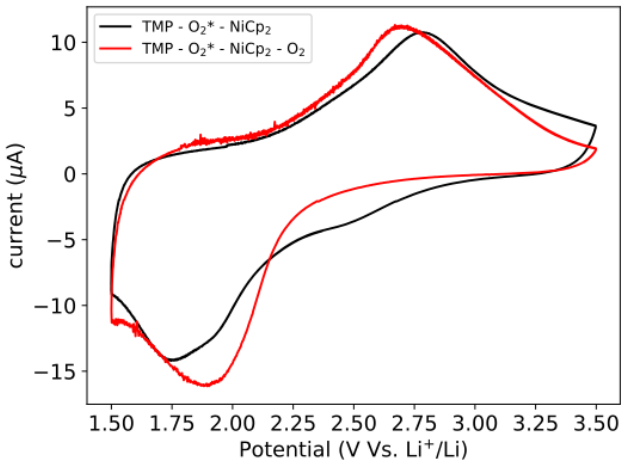

Figure S3: Cyclic voltammogram of nickel phosphate deposited with and without an additional oxygen plasma. The voltammogram is recorded after the electrochemical activation at low potential, and is measured at a scan rate of 1 mv/s.

In addition, the activation of PE-ALD nickel phosphate (without additional oxygen plasma) is also presented, together with several subsequent cycles, in figure S4. Here, the shift of the cathodic peak after activation is clearly visible, as well as the disappearance of the high voltage component of the cathodic peak throughout cycling.

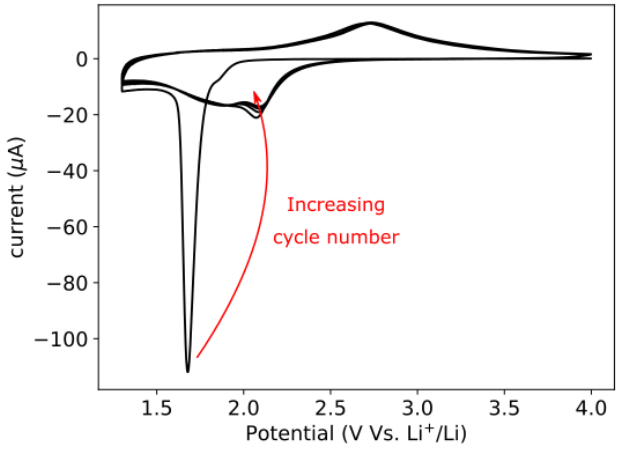

Figure S4: Initial cycles of nickel phosphate, with the red arrow denoting how the cycle number evolves. The voltammogram is measured at a scan rate of 1 mv/s.